aerospace

MDPI

Article

Configuration Stability Analysis for Geocentric Space Gravitational-Wave Observatories

Xingyu Zhou, Feida Jia and Xiangyu Li *

School of Aerospace Engineering, Beijing Institute of Technology, Beijing 100081, China
* Correspondence: lixiangy@bit.edu.cn

Abstract: Long-term configuration stability is essential for a space-based gravitational-wave observatory, which can be affected by orbit insertion errors. This paper investigated the stability of a geocentric gravitational-wave observatory from the view of the configuration uncertainty propagation. The effects of the orbit insertion errors on the configuration stability are propagated using the Unscented Transformation (UT). The best UT tuning factor is selected based on the accuracy analysis of different UT tuning factors. The effects of the position and velocity insertion errors in different directions are firstly discussed. Compared with the Monte Carlo simulations, the UT method has relative errors of no more than 2.7%, while the time cost is only 3.6%. It is found that the radial position and tangential velocity insertion errors have the largest influence on the configuration stability. Finally, based on the proposed method, the stability domain of the geocentric space gravitational-wave detection constellation is investigated by considering two kinds of insertion errors, i.e., independent and identically distributed insertion errors and insertion errors in spatial directions. The analysis results in this paper can be potentially useful for the configuration design of a geocentric gravitational-wave observatory.

Keywords: space-based gravitational-wave observatory; configuration stability; uncertainty propagation; covariance analysis; stability domain

check for updates

Citation: Zhou, X.; Jia, F.; Li, X. Configuration Stability Analysis for Geocentric Space Gravitational-Wave Observatories. *Aerospace* **2022**, *9*, 519. https://doi.org/10.3390/aerospace9090519

Academic Editor: Pierre Rochus

Received: 14 August 2022
Accepted: 14 September 2022
Published: 17 September 2022

1. Introduction

Gravitational-wave detection has become increasingly attractive following the first direct observation made by the Laser Interferometer Gravitational-Wave Observatory (LIGO) [1–4]. The signatures of a gravitational-wave can be detected using a laser interferometer [5–8]. However, due to the limitation of the Earth's curvature and vibration, it is difficult to detect (e.g., LIGO) gravitational-waves with a frequency of lower than 10 Hz [9–13]. Compared with the ground-based observatory, space-based gravitational-wave observatories have much longer arm lengths and are free from the noise related to the seismic and gravity gradient [14–16]. Therefore, space-based gravitational-wave observatories are much more sensitive to low-frequency gravitational-waves, towards which interest and attention have recently been directed [17].

Many space-based gravitational-wave observatories are currently in the development phase of research, such as with the Laser Interferometer Space Antenna (LISA/eLISA) [5,9,18,19], TianQin [12,14,20,21], and TAIJI [13,22–24]. In these planned space-based gravitational-wave observatories, three spacecraft are used; therefore, a triangular configuration is formed. Any one of the three spacecraft can be chosen as the center of the interferometer, while the other two become the endpoints of the two interferometer baselines. The LISA and the TAIJI projects are classic heliocentric designs, with three spacecraft orbiting the Sun [13]. TianQin is another space-based gravitational-wave observatory project put forward by the Sun Yat-sen University in 2016 [12]. Different from the LISA/eLISA and TAIJI projects, the TianQin project is a geocentric gravitational-wave observatory. The TianQin project is a constellation containing three identical drag-free controlled detectors in high Earth orbits with an altitude of 10^5 km [7].

For these mentioned space-based gravitational-wave observatories, long-term configuration stability is usually required to guarantee the performance of interferometric detection. The configuration stability of the space-based gravitational-wave observatories can be measured with three configuration parameters: the arm length, the breathing angle and the relative velocity [24]. The changes in configuration parameters will result in Doppler shift in the laser signals and the beam pointing variations, exceeding the capacity of the detection payloads [7]. The permitted changes in these stability indexes are determined according to the capacity of the scientific payloads, and are taken into consideration when designing and optimizing the orbits. Although the pre-designed and optimized nominal orbits can meet the configuration stability requirements, the long-term behavior of the configuration may still be hazardous due to multiple factors, in which the insertion errors are the most significant ones. Affected by the insertion errors, the spacecraft will deviate from their nominal orbits, and in turn, the long-term stability requirements are no longer satisfied [12,13,25]. Therefore, it is necessary to investigate the configuration uncertainty propagation problems and analyze the influence of the insertion errors on the configuration stability.

Generally, uncertainty propagation is used to characterize the variable's moment (usually represented by mean and covariance matrix) or probability density function (PDF) [26–30]. Various uncertainty propagation methods have been proposed, including Monte Carlo simulations [31,32], the Linear Covariance Analysis (LinCov) [33], the Covariance Analysis Description Equation Technique (CADET) [34], Unscented Transformation (UT) and its variants [35–37], Polynomial Chaos (PC) [38–40], and State Transition Tensors (STT) and its variants [41–43]. These approaches have been well investigated to solve the uncertainty propagation problem in orbital mechanics for a single spacecraft [26,44–46]. Few works focus on the uncertainty propagation problem of a constellation configuration. Li et al. investigated the stability of the heliocentric gravitational detection observatory using the CADET and the UT methods, and some properties were found [13]. The heliocentric gravitational detection observatory is inherently a formation in the heliocentric inertial coordinate, and the motions of the spacecraft can be fully described using the relative dynamic equation. Compared with heliocentric gravitational detection observatories, the geocentric gravitational detection observatory orbits around the Earth, and is classified as the constellation. Therefore, the dynamic environment of the geocentric gravitational detection observatory is different from that of the heliocentric ones, which makes stability properties different. Thus, it is necessary to perform the stability analysis of the geocentric gravitational-wave observatory, and uncover the effects of the insertion errors on the stability of the geocentric gravitational-wave observatory.

This paper focuses on investigating the stability of the geocentric gravitational-wave observatory. The TianQin project is selected as the research object in this paper. The stability domain of the geocentric gravitational-wave observatory is analyzed from the view of the configuration uncertainty propagation. The effects of the insertion errors on the configuration stability are investigated based on the UT method. The accuracy of the UT methods with different UT tuning factors is discussed via a comparison with the Monte Carlo (MC) simulations, and the best UT tuning factors for addressing the configuration uncertainty propagation problem is selected. The effects of the insertion errors in different directions and with different magnitudes are studied. Furthermore, the stability domain, in which the stability requirements are always met, is determined and analyzed. Compared with the configuration uncertainty propagation analysis of the heliocentric designs, some more interesting conclusions are found.

The remainder of this paper is organized as follows. Section 2 begins by describing the configuration design and the dynamic model of the geocentric gravitational-wave observatory. The three stability indexes, i.e., the arm length, the breathing angle and the relative velocity, are presented. Section 3 begins by briefly describing the UT method, followed by an accuracy analysis of the UT method with different UT tuning factors. The effects of the insertion errors in different spatial directions are considered. The stability domain of the geocentric space gravitational detection constellation is computed and analyzed in Section 4. Finally, the conclusions are provided in Section 5.

2. Description of the Geocentric Gravitational Wave Observatory

In this section, the configuration design and dynamic environment of the geocentric gravitational-wave observatory are presented first. Then, the three stability indexes evaluating the performance of the constellation are described in detail.

2.1. Configuration Design and Dynamic Model

As shown in Figure 1, the geocentric gravitational-wave observatory is in an equilateral triangular configuration with three identical drag-free spacecraft orbiting the Earth [26]. The constellation is designed to face the white-dwarf binary RXJ0806.3+1527 (also known as HM Cancri, hereafter referred to as J0806) as a reference source. The symbols 'SC1', 'SC2' and 'SC3' denote the three spacecraft. The orbits of three spacecraft are represented in the heliocentric-ecliptic coordinate system. The nominal orbital elements for three spacecraft in the EarthMJ2000Ec (Keplerian, ecliptic) coordinates are illustrated in Table 1 [7]. The currently planned initial epoch is 22 May 2034 at 12:00:00 UTC. The orbital elements a, e, ν, i, ω and Ω, respectively, label the semimajor axis, eccentricity, true anomaly, inclination, argument of periapsis and longitude of the ascending node, with their definitions shown in Figure 2.

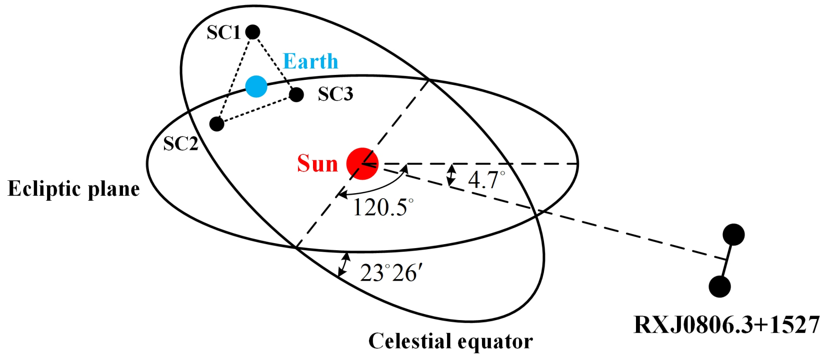

Figure 1. An illustration of the preliminary concept of the geocentric gravitational-wave observatory.

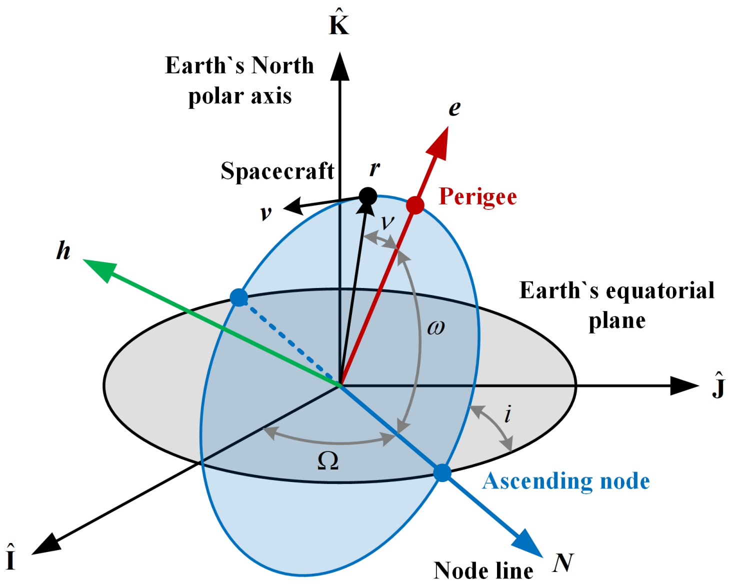

Figure 2. An illustration of the orbit elements.

Table 1. The nominal orbital elements in the EarthMJ2000Ec coordinate at the epoch 22 May 2034 12:00:00 UT [7].

	a/km	e	i/deg	Ω/deg	ω/deg	ν/deg
SC1	99995.57	0.00043	94.69	210.44	358.624	61.32
SC2	100011.4	0.00000	94.70	210.44	0.0000	179.93
SC3	99993.04	0.00031	94.71	210.44	0.0016	299.91

The high-fidelity dynamic model for orbit propagation of the three spacecraft includes the 10×10 spherical-harmonic model of the Earth's gravity field (using JGM-3, JGM-3 denotes the Joint Gravity Model-3 [47]), and the point-mass gravity field from the Moon and Sun (using the ephemeris DE421) [7]. According to [7,12,14], the dynamics of the spacecraft are as follows:

$$\begin{cases} \dot{\boldsymbol{r}}_i = \boldsymbol{v}_i \\ \dot{\boldsymbol{v}}_i = -\frac{\mu_e}{\|\boldsymbol{r}_i\|^3}\boldsymbol{r}_i + \mu_s\left(\frac{\boldsymbol{r}_s - \boldsymbol{r}_i}{\|\boldsymbol{r}_s - \boldsymbol{r}_i\|^3} - \frac{\boldsymbol{r}_s}{\|\boldsymbol{r}_s\|^3}\right) + \mu_m\left(\frac{\boldsymbol{r}_m - \boldsymbol{r}_i}{\|\boldsymbol{r}_m - \boldsymbol{r}_i\|^3} - \frac{\boldsymbol{r}_m}{\|\boldsymbol{r}_m\|^3}\right) + \boldsymbol{a}_{J_{10\times 10}}(\boldsymbol{r}_i) \end{cases} \tag{1}$$

where $\boldsymbol{x}_i = [\boldsymbol{r}_i; \boldsymbol{v}_i] = [x_i, y_i, z_i, \dot{x}_i, \dot{y}_i, \dot{z}_i]^T$ denotes the state of the spacecraft; μ_e, μ_s and μ_m are the gravitational constant of the Earth, the Sun and the Moon, respectively; $\boldsymbol{r}_s$ and $\boldsymbol{r}_m$ label positions of the Sun and Moon relative to the Earth; $\boldsymbol{a}_{J_{10\times 10}}(\cdot)$ is the Earth's 10×10 spherical-harmonic perturbation acceleration.

2.2. Stability Indexes

The three stability indexes related to configuration geometry are used to evaluate the performance of the gravitational-wave observatory constellation [7,13]. The three stability indexes are the arm length l_{ij}, the breathing angle θ_i and the relative velocity $\dot{l}_{ij}$. These indexes can be expressed as:

$$l_{ij} = \|\boldsymbol{r}_{ij}\| \tag{2}$$

$$\theta_i(t) = \arccos\left(\frac{\boldsymbol{r}_{ij}(t) \cdot \boldsymbol{r}_{ik}(t)}{l_{ij}(t) \cdot l_{ik}(t)}\right) \tag{3}$$

$$\dot{l}_{ij}(t) = \frac{\boldsymbol{r}_{ij}(t) \cdot \boldsymbol{v}_{ij}(t)}{\|\boldsymbol{r}_{ij}(t)\|} \tag{4}$$

where $\boldsymbol{r}_{ij} = \boldsymbol{r}_j - \boldsymbol{r}_i$ is the position vector from spacecraft i to spacecraft j.

Figure 3 illustrates the arm length and the breathing angle. The desired values and the permissible variations of the three geometry parameters are listed in Table 2. For the geocentric gravitational-wave observatory, the arm length of the constellation is expected to be maintained at around $\sqrt{3} \times 10^5$ km, with changes of no larger than 1%. The variations of the breathing angle are required to be smaller than 0.2° in the five years. Moreover, the relative velocity should not be larger than 10 m/s within five years. Note that in the mission period, it is assumed there are no orbital maneuvers as the orbital maneuvers will affect the performance of the observatory.

Table 2. The desired value and permitted range of the stability indexes.

Stability Index	Desired Value	Permitted Range
Arm length l_{ij}	$\sqrt{3} \times 10^5$ km	$\pm 1\% \times \sqrt{3} \times 10^5$ km
Breathing angle θ_i	60°	$\pm 0.2°$ for 5 years; $\pm 0.1°$ for the first 2 years
Relative velocity $\dot{l}_{ij}$	0 m/s	± 10 m/s for 5 years; ± 5 m/s for the first 2 years

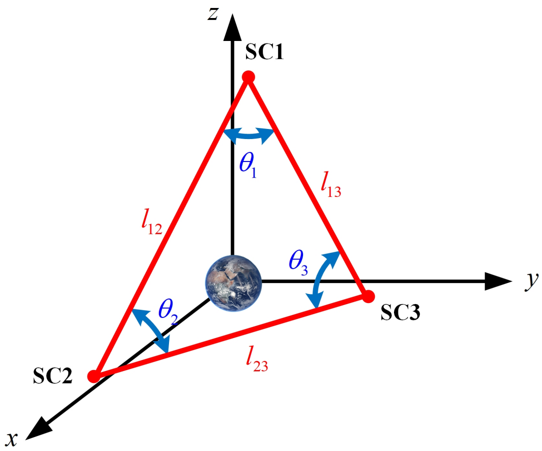

Figure 3. An illustration of the arm length and the breathing angle. SC1, SC2 and SC3, respectively, represent the spacecraft 1, spacecraft 2 and spacecraft 3.

With the dynamics in Equation (1) and the initial states in Table 1, the orbits of the three spacecraft within five years are propagated using a fifth-order RungeKutta integrator with fourth-order error control (RungeKutta45). Under the multiple perturbations, the three stability parameters are not time-varying. The changes of the arm length l_{ij}, the breathing angle θ_i and the relative velocity $\dot{l}_{ij}$ in five years are shown in Figure 4. As shown in Figure 4, the changes of the arm length are no greater than 0.1309% (around 226.8277 km). Furthermore, when the mission lifetime is five years, the maximal changes of the breathing angle and the relative velocity are 0.0949 deg and 4.3614 m/s, respectively.

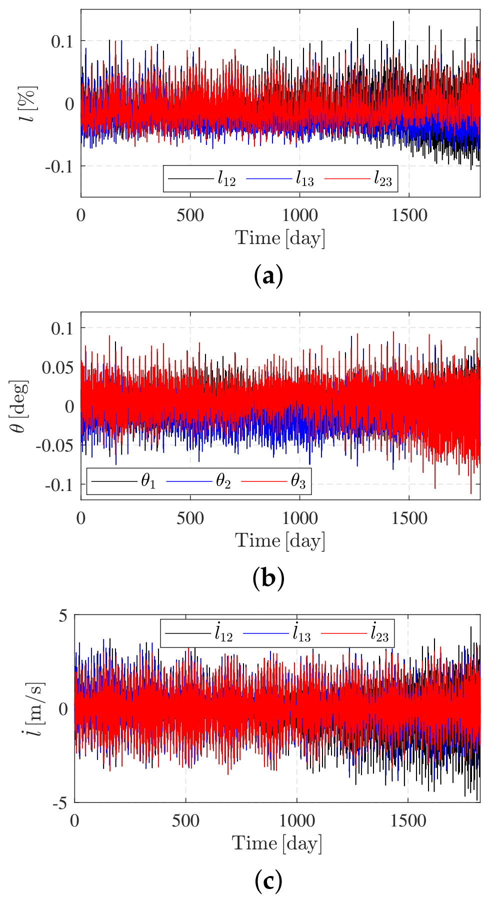

Figure 4. Changes of the stability indexes in a 5-years' lifetime. (**a**) Arm length. (**b**) Breathing angle. (**c**) Relative velocity.

The configuration uncertainty propagation is used to analyze the influence of the initial uncertainty on the constellation geometry. To be specific, it is used to predict the distribution of the three configuration stability indexes $l_{ij}(t)$, $\theta_i(t)$ and $\dot{l}_{ij}(t)$ at any epoch t, with a given initial orbit insertion uncertainty. Usually, the distribution of a random variable can be characterized by its first two moments, i.e., the mean value and the covariance matrix. The distribution assumption can be true for the insertion-errors-propagation problem, as the initial orbit insertion errors are often considered as the Gaussian-distributed errors [13]. The initial orbit insertion uncertainty refers to the orbit insertion errors in the EarthMJ2000Eq coordinate. Let $\bar{x}_i^0 \in \mathbb{R}^6$ and $\boldsymbol{P}_i^0 \in \mathbb{R}^{6\times 6}$ be the mean value and the covariance matrix of the i-th spacecraft's insertion state (i.e., $\boldsymbol{x}_i^0$), respectively, and the mean values and the covariance matrices of the stability indexes are written as follows:

$$[\bar{\boldsymbol{y}}(t), \boldsymbol{P}(\boldsymbol{y}(t))] = \mathrm{UP}\left(\bar{x}_1^0, \boldsymbol{P}_1^0, \bar{x}_2^0, \boldsymbol{P}_2^0, \bar{x}_3^0, \boldsymbol{P}_3^0, t\right) \tag{5}$$

where $\boldsymbol{y} = [l_{12}, l_{13}, l_{23}, \theta_1, \theta_2, \theta_3, \dot{l}_{12}, \dot{l}_{13}, \dot{l}_{23}]^T$ is the vector of the stability indexes; $\bar{\boldsymbol{y}}(t) \in \mathbb{R}^9$ and $\boldsymbol{P}(\boldsymbol{y}(t)) \in \mathbb{R}^{9\times 9}$ are the mean and covariance matrix of the stability index vector $\boldsymbol{y}(t)$; $\mathrm{UP}(\cdot)$ denotes the uncertainty propagation process. The method for predicting the mean $\bar{\boldsymbol{y}}(t)$ and covariance matrix $\boldsymbol{P}(\boldsymbol{y}(t))$ will be detailed in Section 3.

3. Configuration Uncertainty Propagation Based on UT Method

This section begins with a brief review of the UT method, followed by the accuracy of the UT method using different tuning factors which are analyzed in Section 3.2. The best UT tuning factors are determined. Finally, the characteristics of the configuration uncertainty propagation of the geocentric gravitational-wave observatory is analyzed based on the UT method.

3.1. Unscented Transformation Method

According to Equations (1)–(4), the transformation from the orbit insertion state $\boldsymbol{X} = [\boldsymbol{x}_1^0; \boldsymbol{x}_2^0; \boldsymbol{x}_3^0]$ to the stability indexes $\boldsymbol{y}(t)$ is nonlinear, which has two distinctive features. The first is that this transformation is a black-box model, which has no analytical solutions. Therefore, analytical uncertainty propagation methods, such as the CADET or STT, are not appropriate for solving the configuration uncertainty propagation. The second feature is that the calculation of this transformation is an expensive process as long-term numerical integration is required.

The sigma-point based methods allow for the use of already existing propagation tools as a black-box and avoids any analytical solutions or gradient information, which can be conveniently extended to solve the configuration problem. The widely used sigma-point methods include the UT method, Conjugate Unscented Transform (CUT) and Cubature rules (CRs). These sigma-point methods approximate the probability distribution at a future time by nonlinearly integrating a few sigma-samples, which are deterministically selected according to the given initial distribution. Among these sigma-point methods, the UT method has less computational overhead and has been successfully applied to solve the configuration uncertainty propagation problem of a heliocentric gravitational-wave observatory (the TAIJI project). Thus, considering the factors of time, cost and convenience, the UT is used in this paper.

The schematic diagram of the UT method is illustrated in Figure 5. Consider the random variable $\boldsymbol{X}$ with the mean $\bar{\boldsymbol{X}}$ and covariance $\boldsymbol{P_X}$ as follows:

$$\bar{\boldsymbol{X}} = [\bar{x}_1^0; \bar{x}_2^0; \bar{x}_3^0] \tag{6}$$

$$\boldsymbol{P_X} = \begin{bmatrix} \boldsymbol{P}_1^0 & \boldsymbol{0}_{6\times 6} & \boldsymbol{0}_{6\times 6} \\ \boldsymbol{0}_{6\times 6} & \boldsymbol{P}_2^0 & \boldsymbol{0}_{6\times 6} \\ \boldsymbol{0}_{6\times 6} & \boldsymbol{0}_{6\times 6} & \boldsymbol{P}_3^0 \end{bmatrix} \tag{7}$$

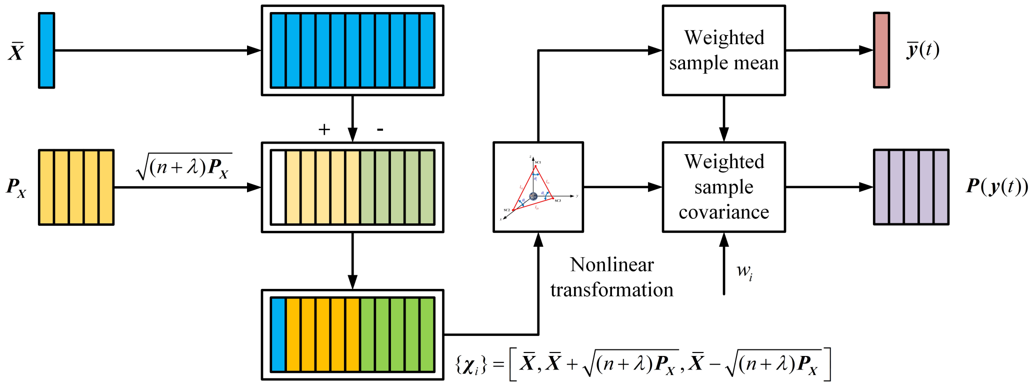

Figure 5. A schematic diagram of the unscented transformation. $\boldsymbol{x}$ and $\boldsymbol{y}$ denote the input and output variables, respectively.

According to the mean $\bar{\boldsymbol{X}}$ and covariance $\boldsymbol{P_X}$, the sigma-point set $\{\chi_i\}$ is then formulated as:

$$\begin{aligned} \chi_i &= \bar{\boldsymbol{X}} \quad i \in \{0\} \\ \chi_i &= \bar{\boldsymbol{X}} + \left[\sqrt{(n+\lambda)\boldsymbol{P_X}}\right]_i \quad i \in \{1,2,\cdots,n\} \\ \chi_i &= \bar{\boldsymbol{X}} - \left[\sqrt{(n+\lambda)\boldsymbol{P_X}}\right]_i \quad i \in \{n+1,n+2,\cdots,2n\} \end{aligned} \tag{8}$$

where $n = 18$ is the dimension of the variable $\boldsymbol{X}$; $[\cdot]_i$ denotes the i-th column of the matrix; λ is an adjusting dispersion parameter called the UT tuning factor; and $\sqrt{\boldsymbol{P_X}}$ can be obtained using the Cholesky decomposition, which satisfies $\boldsymbol{P_X} = \sqrt{\boldsymbol{P_X}}\left(\sqrt{\boldsymbol{P_X}}\right)^T$.

The weights of the i-th sigma points χ_i are obtained as follows:

$$\begin{aligned} w_i &= \frac{\lambda}{\lambda+n} \quad i \in \{0\} \\ w_i &= \frac{1}{2(\lambda+n)} \quad i \in \{1,2,\cdots,2n\} \end{aligned} \tag{9}$$

For each orbit insertion state χ_i, the orbits of the three spacecraft are propagated using the RungeKutta45 method; then, the corresponding stability indexes $\boldsymbol{y}_i(t)$ are obtained according to Equations (2)–(4). According to the UT method, the mean $\bar{\boldsymbol{y}}(t)$ and covariance matrix $\boldsymbol{P}(\boldsymbol{y}(t))$ of the stability indexes are approximated by

$$\bar{\boldsymbol{y}}(t) = \sum_{i=0}^{2n} w_i \boldsymbol{y}_i(t) \tag{10}$$

$$\boldsymbol{P}(\boldsymbol{y}(t)) = \sum_{i=0}^{2n} w_i [\boldsymbol{y}_i(t) - \bar{\boldsymbol{y}}(t)][\boldsymbol{y}_i(t) - \bar{\boldsymbol{y}}(t)]^T \tag{11}$$

According to the equations above, the distributions of the stability indexes of any time in the mission lifetime can be obtained by calculating 37 sigma points.

3.2. Selection of the UT Tuning Factor

In this subsection, the accuracy of the UT method is analyzed. To use the UT method, the UT tuning factor λ should be carefully selected. In [13], the value of λ is selected as $3 - n$, for which the selection followed from the recommendation in Julier and Uhlmann that $n + \lambda = 3$ [35]. In this case, the kurtosis of one state of the sigma points agrees with that of the Gaussian distribution. However, for high-dimensional problems such as the configuration uncertainty propagation, this value produces a negative weight at the mean, which may adversely affect the performance of the UT. Therefore, it is worth testing the UT methods with different tuning factors and comparing the performances.

For simplicity, $\kappa = \lambda + n$ denotes the variable related to the UT tuning factor. A total of nine UT methods are tested, with the variable $\kappa \in \{1, 2, 3, 8, 9, 10, 17, 18, 19\}$. Two cases, including a standard case and a severe case, are simulated to verify the performance of the UT methods with different tuning factors. The standard deviation (STD) of the insertion errors of the two cases are listed in Table 3. The covariance matrix of the insertion errors of the standard case is written as:

$$\boldsymbol{P}_1^0 = \boldsymbol{P}_2^0 = \boldsymbol{P}_3^0 = \begin{bmatrix} 100\mathbf{I}_3 \text{ m}^2 & \mathbf{0}_{3\times3} \\ \mathbf{0}_{3\times3} & 100\mathbf{I}_3 \text{ mm}^2/s^2 \end{bmatrix} \tag{12}$$

where $\mathbf{I}_3 \in \mathbb{R}^{3\times3}$ denotes the 3-dimensional identified matrix.

According to Table 3, for the severe case, the covariance matrix of the insertion errors is partitioned as:

$$\boldsymbol{P}_1^0 = \boldsymbol{P}_2^0 = \boldsymbol{P}_3^0 = \begin{bmatrix} 10000\mathbf{I}_3 \text{ m}^2 & \mathbf{0}_{3\times3} \\ \mathbf{0}_{3\times3} & 100\mathbf{I}_3 \text{ cm}^2/s^2 \end{bmatrix} \tag{13}$$

Table 3. The STDs of the insertion errors of the simulated cases.

	Initial Position Errors	**Initial Velocity Errors**
Standard case	10 m per axis	10 mm/s per axis
Severe case	100 m per axis	100 mm/s per axis

The results predicted by the UT methods are compared with the Monte Carlo simulation method. The number of the samples used in the Monte Carlo simulation is set to 1000. Taken the covariance predicted by the Monte Carlo simulation as a standard, the relative error of the covariance obtained by the UT methods is defined as:

$$\eta(t) = \frac{\|\boldsymbol{P}_{UT}(t) - \boldsymbol{P}_{MC}(t)\|}{\|\boldsymbol{P}_{MC}(t)\|} \tag{14}$$

where $\eta(t)$ is the defined relative errors of two matrices; $\boldsymbol{P}_{MC}(t)$ and $\boldsymbol{P}_{UT}(t)$ are the covariance matrices calculated by the Monte Carlo simulation and UT methods at the epoch t, respectively; and $\|\cdot\|$ represents the Frobenius norm (sum square of the elements). The smaller the $\eta(t)$, the better the performance.

The relative errors $\eta(t)$ of the UT methods using different tuning factors are computed. For each UT tuning factor, the relative errors at 11 epochs are tested. The testing epochs begin at 0 and end at 5 years, with a time interval of 0.5 years. The average relative errors of the 11 epochs of different UT methods are listed in Table 4. For the standard case, the nine UT methods possess a similar performance. However, for the severe case, the performances of the nine UT methods differ. For example, the relative error of the UT method $\kappa = 9$ is around 0.1103, while for the UT method $\kappa = 19$, the relative error is around 0.2188. To better compare the performance of different UT methods in predicting the covariance of the three stability indexes, a weighted index is proposed by combing the relative errors of the arm length, the breathing angle and the relative velocity as follows:

$$\bar{\eta} = \frac{\eta(l) + \eta(\theta) + \eta(\dot{l})}{3} \tag{15}$$

where $\bar{\eta}$ denotes the weighted relative error. The values of the weighted relative errors of different UT methods are also listed in Table 4. The UT method with a tuning factor λ of equal to -9 ($\kappa = 9$) has the smallest relative errors; therefore, in this paper, $\lambda = -9$ is selected as the UT tuning factor for the following analysis.

Table 4. Accuracy test results of the UT methods with different tuning factors.

κ	$\lambda = \kappa - n$	Standard Case				Severe Case			
		$\eta(l)$	$\eta(\theta)$	$\eta(\dot{l})$	$\bar{\eta}$	$\eta(l)$	$\eta(\theta)$	$\eta(\dot{l})$	$\bar{\eta}$
1	−17	0.0261	0.0239	0.0425	0.0308	0.1141	0.0499	0.1285	0.0975
2	−16	0.0261	0.0239	0.0425	0.0308	0.1074	0.0499	0.1136	0.0903
3	−15	0.0261	0.0239	0.0425	0.0308	0.1012	0.0499	0.1129	0.0880
8	−10	0.0261	0.0239	0.0424	0.0308	0.0781	0.0499	0.1135	0.0805
9	−9	0.0261	0.0239	0.0424	0.0308	0.0760	0.0499	0.1103	0.0787
10	−8	0.0262	0.0239	0.0424	0.0308	0.0751	0.0499	0.1186	0.0812
17	−1	0.0262	0.0239	0.0425	0.0309	0.0954	0.0499	0.1954	0.1136
18	0	0.0263	0.0239	0.0425	0.0309	0.1005	0.0499	0.2071	0.1192
19	1	0.0263	0.0239	0.0424	0.0309	0.1058	0.0499	0.2188	0.1248

Figure 6 shows the STD results of the standard case obtained by the UT method ($\kappa = 9$), and the results are compared with those obtained by the Monte Carlo simulation (1000 samples). The blue lines represent the results of Monte Carlo and the red dashed lines represent the results obtained by the UT. Moreover, the predicted stability indexes' uncertainties at epoch $t = 5$ years, are illustrated in Figure 7. The corresponding means and the 3σ ellipsoid bounds are projected. In addition, for the sake of comparison, 1000 Monte Carlo samples are plotted the grey 'x'. The mean and the 3σ ellipsoid bounds obtained by the Monte Carlo simulation are shown by the blue squares and blue dashed lines. It can be seen that the UT method can accurately represent the curvature exhibited by the Monte Carlo samples and the predicted 3σ bounds are very close to that of the Monte Carlo simulation. The STDs of the three stability indexes at the epoch $t = 5$ year predicted by the UT and Monte Carlo simulation are shown in Table 5. It can be found that compared with the Monte Carlo simulation, the UT can predict the STDs with errors of no more than 2.7%.

Table 5. STD comparison of the UT ($\kappa = 9$) and the Monte Carlo simulation.

		Monte Carlo	UT	RE/%
Arm length/km	l_{12}	3342.7926	3338.7718	0.1202
	l_{13}	3340.4763	3340.7576	0.0084
	l_{23}	3412.3042	3340.1915	2.1133
Breathing angle/°	θ_1	1.9427	1.9129	1.5306
	θ_2	1.9084	1.9138	0.2831
	θ_3	1.9190	1.9137	0.2794
Relative velocity/(m/s)	$\dot{l}_{12}$	0.2094	0.2037	2.7001
	$\dot{l}_{13}$	0.2513	0.2517	0.1638
	$\dot{l}_{23}$	0.2089	0.2118	1.3645

The simulations were performed using MATLAB R2018b on a computer with a 3.6 GHz AMD Ryzen processor and 16 GB RAM. As shown in Table 6, with the 1000 samples (including 3000 orbits) made for the Monte Carlo simulation, it takes about 9728.3374 s (around 2.7 h). However, the computational time of the UT method is only 347.2791 s (around 5.8 min), which is only 3.5697% that of the Monte Carlo simulations.

Table 6. Run time of a 5-year configuration uncertainty propagation.

Methods	Number of the Orbital Propagation	Time Consumption
Monte Carlo simulation (with 1000 samples)	3000 (1000 samples and each contains three spacecraft)	9728.3374 s (around 2.7 h)
UT ($\kappa = 9$)	111 (37 sigma points and each contain three spacecraft)	347.2791 s (around 5.8 min)

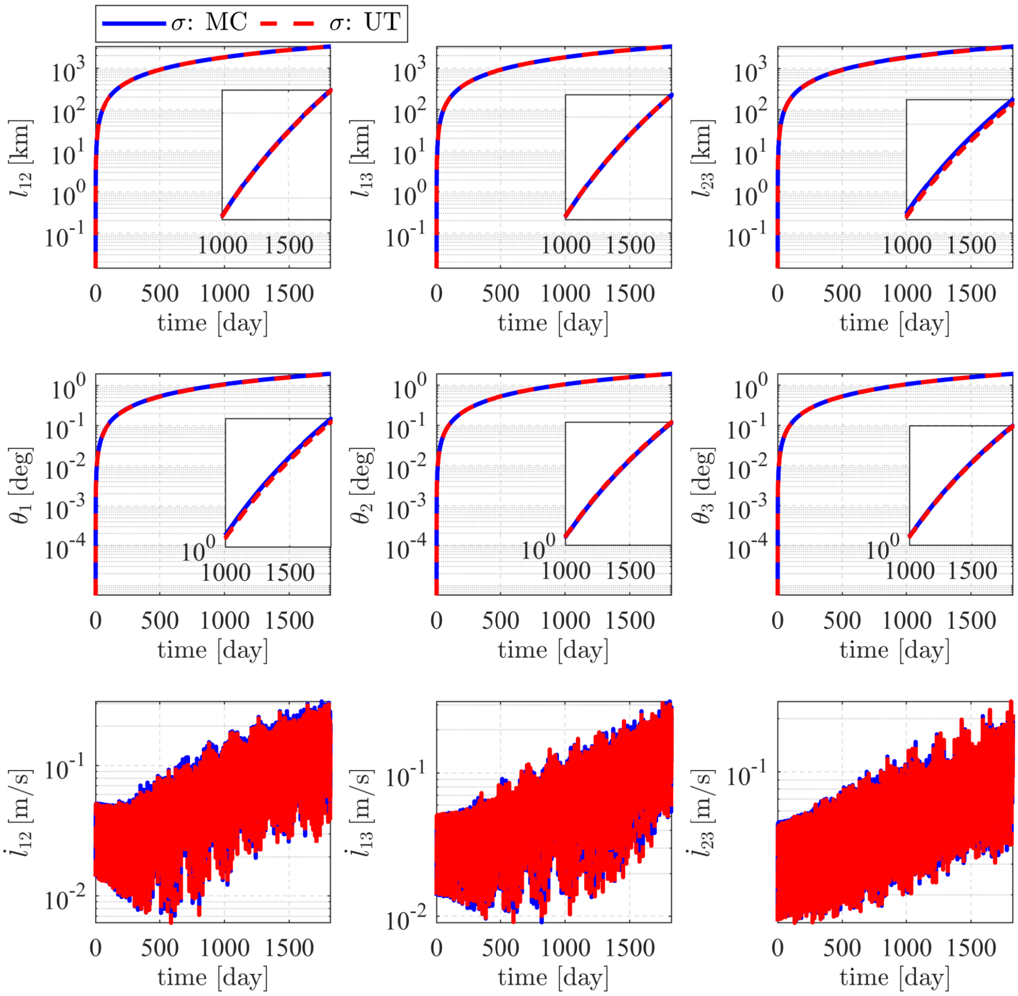

Figure 6. Comparison diagram of the UT ($\kappa = 9$) and the Monte Carlo simulation. The blue lines and the red dashed lines respectively represent the results of the MC simulation and UT method.

3.3. Configuration Uncertainty Propagation Analysis for the Geocentric Space Gravitational Wave Detection Constellation

The effects of the insertion errors in different directions are investigated using the UT method. For an uncertainty variable $\delta \boldsymbol{p} \in \mathbb{R}^m$, given a certain direction $\boldsymbol{d} = [d_1, \cdots, d_m]^T$ and the standard deviation σ_p, the corresponding covariance matrix of $\delta \boldsymbol{p}$ is written as:

$$\boldsymbol{P}(\delta \boldsymbol{p}) = \sigma_p^2 \boldsymbol{d}\boldsymbol{d}^T \tag{16}$$

The radial, tangential and normal position and velocity insertion errors are considered. For radial position and velocity uncertainty, the covariance matrices are obtained as follows:

$$\boldsymbol{P}\left(\boldsymbol{r}_i^0\right) = \sigma_r^2 \frac{\boldsymbol{r}_i^0}{\left\|\boldsymbol{r}_i^0\right\|} \frac{\left(\boldsymbol{r}_i^0\right)^T}{\left\|\boldsymbol{r}_i^0\right\|} \tag{17}$$

$$\boldsymbol{P}\left(\boldsymbol{v}_i^0\right) = \sigma_v^2 \frac{\boldsymbol{r}_i^0}{\left\|\boldsymbol{r}_i^0\right\|} \frac{\left(\boldsymbol{r}_i^0\right)^T}{\left\|\boldsymbol{r}_i^0\right\|} \tag{18}$$

For tangential position and velocity uncertainty:

$$\boldsymbol{P}\left(\boldsymbol{r}_i^0\right) = \sigma_r^2 \frac{\boldsymbol{v}_i^0}{\left\|\boldsymbol{v}_i^0\right\|} \frac{\left(\boldsymbol{v}_i^0\right)^T}{\left\|\boldsymbol{v}_i^0\right\|} \tag{19}$$

$$\boldsymbol{P}\left(\boldsymbol{v}_i^0\right) = \sigma_v^2 \frac{\boldsymbol{v}_i^0}{\left\|\boldsymbol{v}_i^0\right\|} \frac{\left(\boldsymbol{v}_i^0\right)^T}{\left\|\boldsymbol{v}_i^0\right\|} \tag{20}$$

Additionally, for normal position and velocity uncertainty:

$$\boldsymbol{P}\left(\boldsymbol{r}_i^0\right) = \sigma_r^2 \frac{\boldsymbol{r}_i^0 \times \boldsymbol{v}_i^0}{\left\|\boldsymbol{r}_i^0 \times \boldsymbol{v}_i^0\right\|} \frac{\left(\boldsymbol{r}_i^0 \times \boldsymbol{v}_i^0\right)^T}{\left\|\boldsymbol{r}_i^0 \times \boldsymbol{v}_i^0\right\|} \tag{21}$$

$$\boldsymbol{P}\left(\boldsymbol{v}_i^0\right) = \sigma_v^2 \frac{\boldsymbol{r}_i^0 \times \boldsymbol{v}_i^0}{\left\|\boldsymbol{r}_i^0 \times \boldsymbol{v}_i^0\right\|} \frac{\left(\boldsymbol{r}_i^0 \times \boldsymbol{v}_i^0\right)^T}{\left\|\boldsymbol{r}_i^0 \times \boldsymbol{v}_i^0\right\|} \tag{22}$$

where σ_r and σ_v represent the STD of the position and velocity insertion errors, respectively.

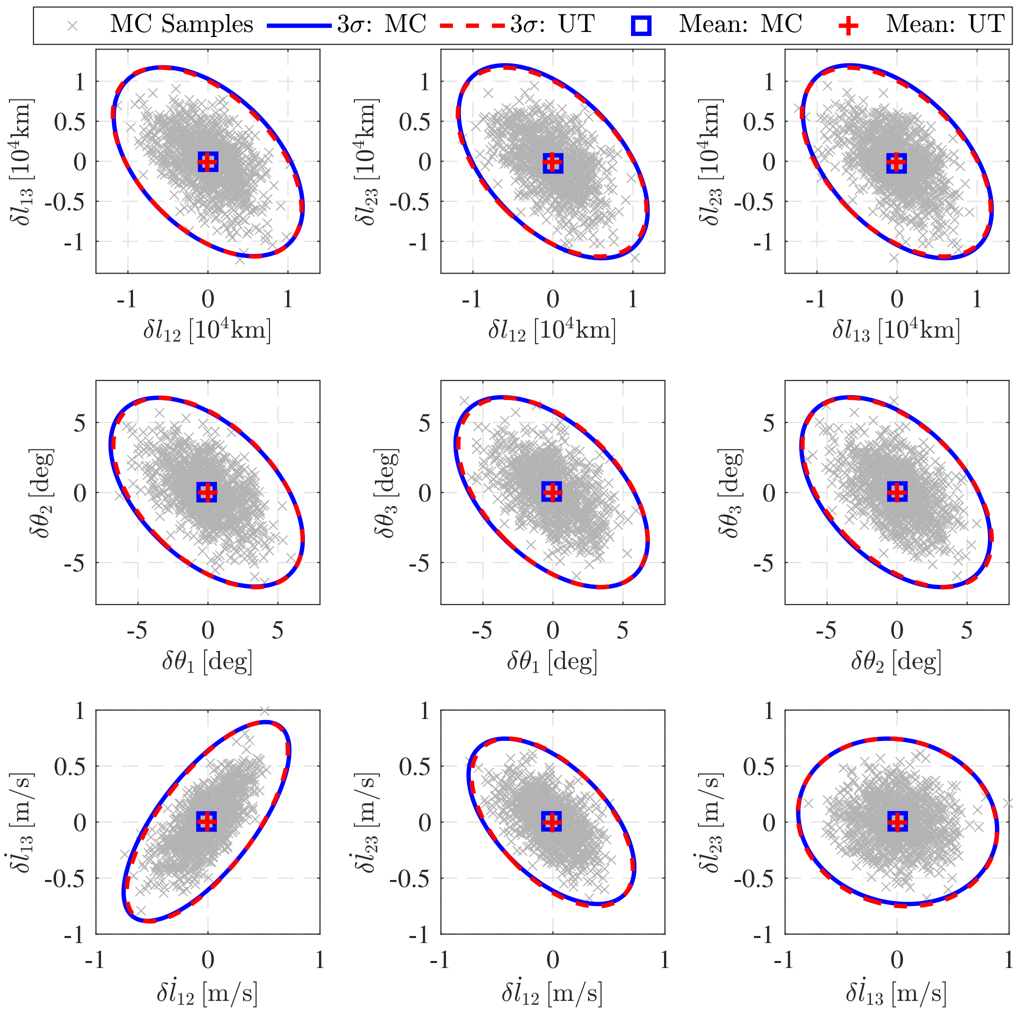

Figure 7. Comparison of the distribution of the stability indexes predicted by the UT ($\kappa = 9$) and the Monte Carlo simulation. The blue lines and the red dashed lines respectively represent the 3σ bounds predicted by the MC simulation and UT method.

Note that to use the UT method, Cholesky decomposition is required to calculate the matrix $\sqrt{\boldsymbol{P_X}}$. To avoid numerical singularity, an identified matrix with tiny values is added to the matrix $\boldsymbol{P_X}$. For example, for the condition that only radial position insertion errors exist, the covariance matrix $\boldsymbol{P_X}$ is obtained as follows:

$$\boldsymbol{P_X} = \begin{bmatrix} \sigma_r^2 \frac{r_1^0 (r_1^0)^T}{\|r_1^0\|^2} & \mathbf{0}_{3\times3} & \mathbf{0}_{3\times3} & \mathbf{0}_{3\times3} & \mathbf{0}_{3\times3} & \mathbf{0}_{3\times3} \\ \mathbf{0}_{3\times3} & \mathbf{0}_{3\times3} & \mathbf{0}_{3\times3} & \mathbf{0}_{3\times3} & \mathbf{0}_{3\times3} & \mathbf{0}_{3\times3} \\ \mathbf{0}_{3\times3} & \mathbf{0}_{3\times3} & \sigma_r^2 \frac{r_2^0 (r_2^0)^T}{\|r_2^0\|^2} & \mathbf{0}_{3\times3} & \mathbf{0}_{3\times3} & \mathbf{0}_{3\times3} \\ \mathbf{0}_{3\times3} & \mathbf{0}_{3\times3} & \mathbf{0}_{3\times3} & \mathbf{0}_{3\times3} & \mathbf{0}_{3\times3} & \mathbf{0}_{3\times3} \\ \mathbf{0}_{3\times3} & \mathbf{0}_{3\times3} & \mathbf{0}_{3\times3} & \mathbf{0}_{3\times3} & \sigma_r^2 \frac{r_3^0 (r_3^0)^T}{\|r_3^0\|^2} & \mathbf{0}_{3\times3} \\ \mathbf{0}_{3\times3} & \mathbf{0}_{3\times3} & \mathbf{0}_{3\times3} & \mathbf{0}_{3\times3} & \mathbf{0}_{3\times3} & \mathbf{0}_{3\times3} \end{bmatrix} + 10^{-16}\mathbf{I}_{18} \tag{23}$$

where $\mathbf{I}_{18} \in \mathbb{R}^{18\times18}$ is an 18-dimensional identified matrix.

First, the configuration stability considering only the insertion errors of spacecraft 1 is investigated. When we consider the effects of the position insertion errors of spacecraft 1 in different directions, only three variables are included, which can be plotted using a three-dimensional figure.

The effects of the position and velocity insertion errors on the stability indexes are studied independently. Assume that the STD of the position and velocity insertion error are 100 m and 0.001 m/s, respectively. A myriad of directions are generated, and for each direction, configuration uncertainty propagation is performed based on the UT method. The results are shown in Figures 8 and 9. In Figures 8 and 9, $\boldsymbol{n} = [n_x, n_y, n_z]^T$ denotes the direction of the insertion errors and each point on the united sphere denotes a spatial direction, and the predicted STD of the arm length is represented by the color. For better comparison, the radial, the tangential and the normal directions are labeled by the blue ($\boldsymbol{d}_1$), red ($\boldsymbol{d}_2$) and green ($\boldsymbol{d}_3$) lines, respectively, in Figures 8 and 9. It can be seen that the effects of the radial position insertion errors and the tangential velocity insertion errors are much more significant than the insertion errors in other directions.

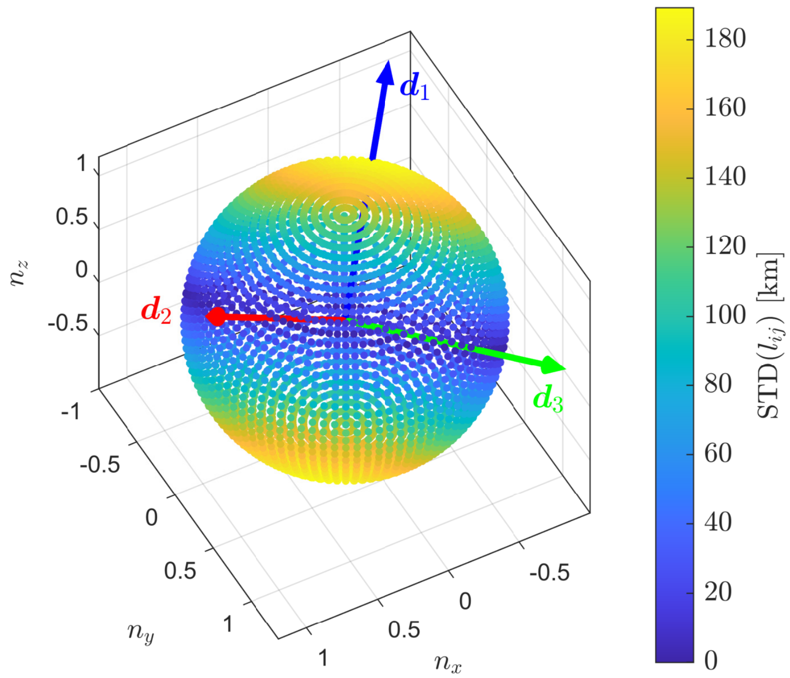

Figure 8. The effects of the position insertion errors of SC1 on the configuration stability. $\boldsymbol{d}_1$, $\boldsymbol{d}_2$ and $\boldsymbol{d}_3$ represent the radial, the tangential and the normal directions, respectively.

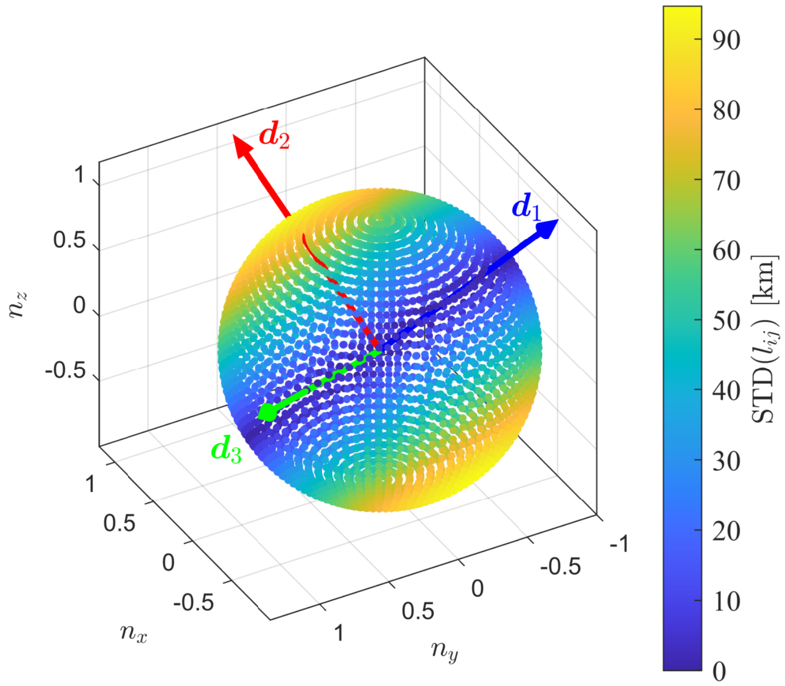

Figure 9. The effects of the velocity insertion errors of SC1 on the configuration stability. $\boldsymbol{d}_1$, $\boldsymbol{d}_2$ and $\boldsymbol{d}_3$ respectively represent the radial, the tangential and the normal directions.

According to the parameter setting in the standard case in Table 3, let $\sigma_r = 10$ m and $\sigma_v = 10$ mm/s. The effects of the radial, tangential and normal position insertion errors on the stability indexes are shown in Figure 10 and Table 7. Figure 10 illustrates the time history of the STDs of the arm length, the breathing angle and the relative velocity considering only the position insertion errors. Table 7 lists the STDs of the three stability indexes at the epoch year under the position insertion errors in different directions. It is found that the arm length and the breathing angle are mainly affected by the radial position insertion errors. The arm length STDs under radial position errors are around 66.8 km, which is about 20 times that under tangential and normal position insertion errors (around 3.34 km).Furthermore, the relative velocity is mainly affected by the radial position insertion errors, and is greatly influenced by the tangential position insertion errors. Among the three directions, the normal position insertion errors have the least effect on the three stability indexes.

Table 7. STDs of the three stability indexes considering position insertion errors in different directions.

		Radial	Tangential	Normal
Arm length/km	l_{12}	66.7896	3.3390	3.3387
	l_{13}	66.8430	3.3412	3.3409
	l_{23}	66.8267	3.3414	3.3402
Breathing angle/°	θ_1	0.0382	0.0019	0.0019
	θ_2	0.0382	0.0019	0.0019
	θ_3	0.0382	0.0019	0.0019
Relative velocity/(m/s)	$\dot{l}_{12}$	0.0035	0.0008	2.0383×10^{-4}
	$\dot{l}_{13}$	0.0032	0.0013	2.5182×10^{-4}
	$\dot{l}_{23}$	0.0034	0.0011	2.1227×10^{-4}

The effects of the radial, tangential and normal velocity insertion errors on the stability indexes are shown in Figure 11 and Table 8. It can be seen that the tangential velocity insertion errors have strong influences on the arm length, the breathing angle and the relative velocity. The normal velocity insertion errors have moderate effects on the relative velocity.

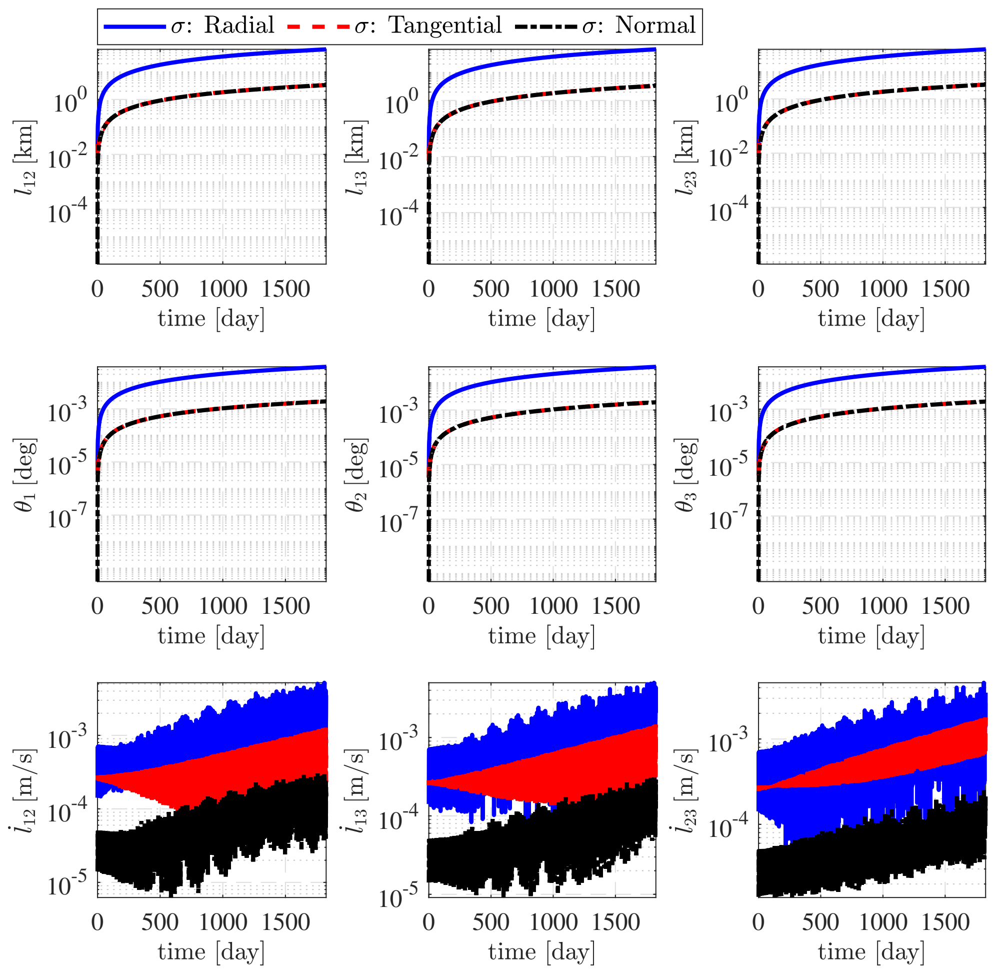

Figure 10. Effects of position insertion errors in different directions.

Table 8. STDs of the three stability indexes considering velocity insertion errors in different directions.

		Radial	**Tangential**	**Normal**
Arm length/km	l_{12}	3.9615	3338.5467	3.3413
	l_{13}	3.8673	3340.7479	3.3457
	l_{23}	5.3745	3339.9500	3.3429
Breathing angle/°	θ_1	0.0025	1.9125	0.0019
	θ_2	0.0025	1.9134	0.0019
	θ_3	0.0020	1.9133	0.0019
Relative velocity/(m/s)	$\dot{l}_{12}$	0.0428	0.1994	3.2657×10^{-4}
	$\dot{l}_{13}$	0.0666	0.2427	3.4147×10^{-4}
	$\dot{l}_{23}$	0.0557	0.2042	3.4498×10^{-4}

According to the above discussion, the effects of the position and velocity insertion errors in different directions are summarized as follows. The radial position insertion errors and the tangential velocity insertion errors strongly affect the three stability parameters. The tangential position insertion errors and radial velocity insertion errors only affect the relative velocity. Moreover, the normal insertion errors have almost no effect on the three stability parameters. The effects of the radial position insertion errors and the tangential velocity insertion errors can be explained as follows. The radial position and the tangential velocity deviation will directly affect the potential energy and kinetic energy of the spacecraft, which causes the orbital period of the spacecraft to be at variance with another spacecraft in the constellation. The phase difference between two spacecraft deviates in the long-term; as a result, the desired regular triangle configuration is impacted. In this case, the arm length and the breathing angle change considerably. However, the insertion errors in other directions only change the spacecraft's orbital plane, which almost has no influence on the configuration.

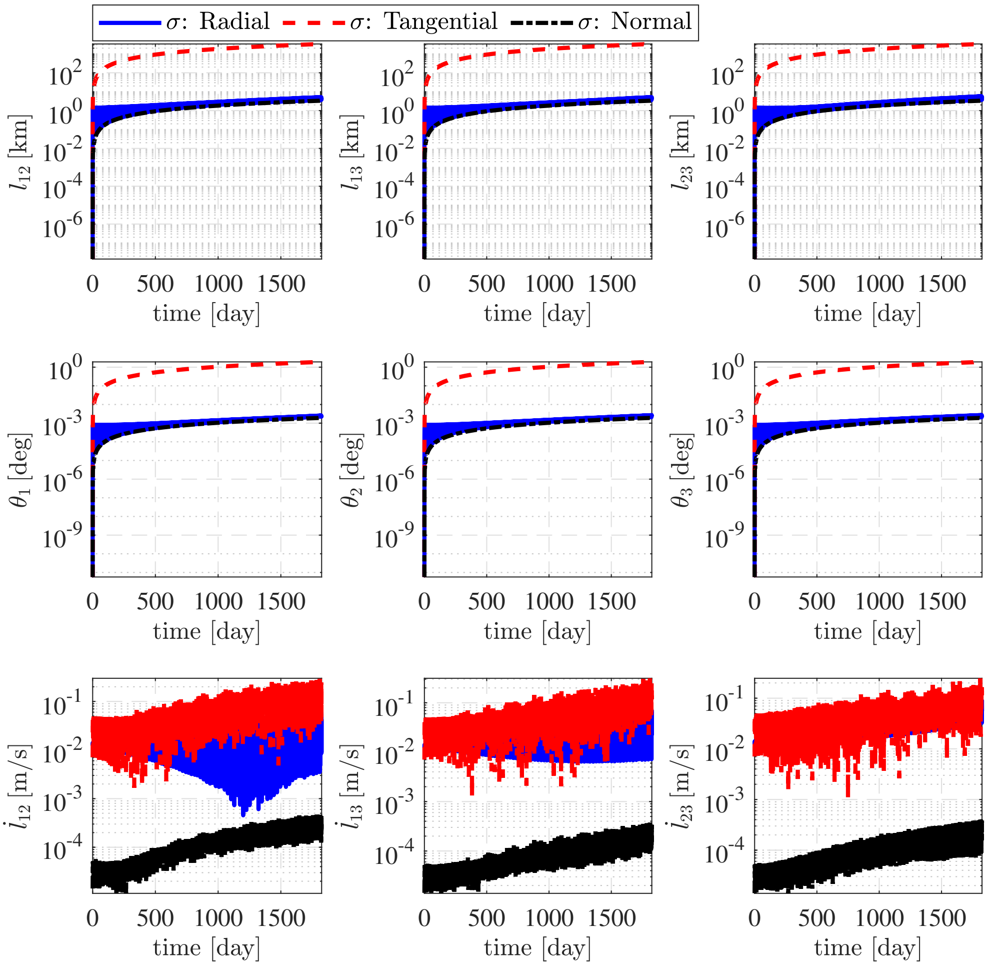

Figure 11. Effects of velocity insertion errors in different directions.

4. Stability Domain Analysis for the Geocentric Space Gravitational Wave Detection Constellation

This section provides the stability domain analysis for the geocentric space gravitational-wave detection constellation. First, the stability domain is analyzed by considering the independent and identically distributed insertion errors in position and velocity. Moreover, following the studies on the effects of uncertainty in different directions in Section 3.3, the stability domains with uncertainty in spatial directions are investigated.

The independent and identically distributed insertion errors are firstly considered. For a case where the STD of the position insertion errors along three axes of the three spacecraft gradually increase from 30 m to 300 m, and the STD of the velocity insertion error increases from 0.5 mm/s to 5 mm/s, the maximal STDs of the arm length, the breathing angle and the relative velocity within three months are shown in Figures 12–14. For the case where the STD of the position insertion error equals 300 m and the STD of the velocity insertion error equals 5 mm/s, the maximal STDs of the arm length, the breathing angle and the relative velocity are 129.4790 km, 0.0742 deg and 0.0289 m/s, respectively. According to the permitted ranges of the three stability indexes listed in Table 2, it is found that the breathing angle is most likely to exceed the stability constraint.

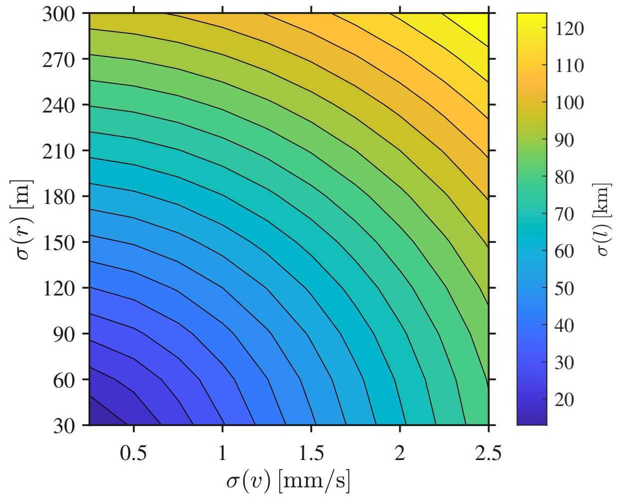

Figure 12. Effects of position and velocity errors on the arm length (three months' propagation).

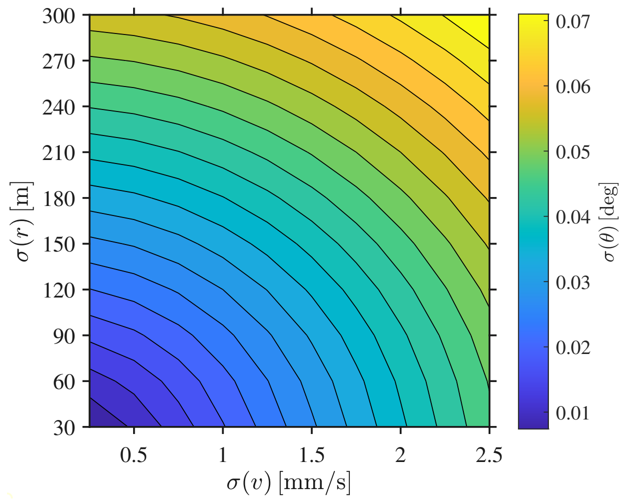

Figure 13. Effects of position and velocity errors on the breathing angle (three months' propagation).

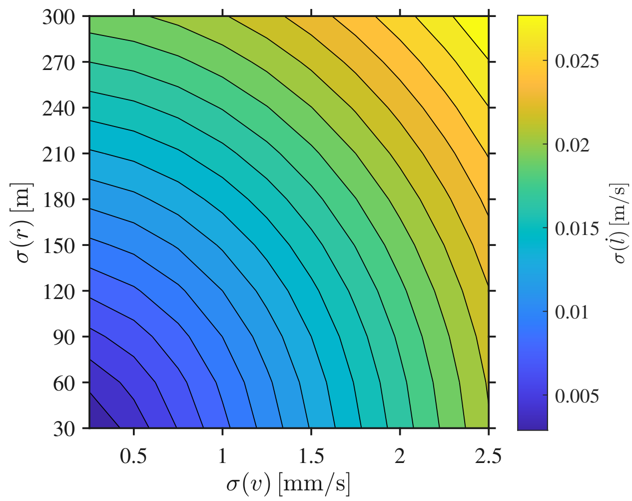

Figure 14. Effects of position and velocity errors on the relative velocity (three months' propagation).

According to the predictions in Figures 12–14 and the stability constraints in Table 2, the stability domain (inside the constraints) for a three-month propagation is determined and shown in Table 9. For the three-month propagation, the insertions errors inside the constraints should satisfy the following equations:

$$3\sigma(l) \leq 1\% \times \left(\sqrt{3} \times 10^5\right)\mathrm{km} \tag{24}$$

$$3\sigma(\theta) \leq 0.1^\circ \tag{25}$$

$$3\sigma(\dot{l}) \leq 5\ \mathrm{m/s} \tag{26}$$

The stability domains of the three-month propagation considering only radial insertion errors (i.e., the radial position insertion errors and the radial velocity insertion errors) were calculated; however, only tangential insertion errors and normal insertion errors are shown in Table 9. It can be seen that when considering only radial insertion errors, if the position insertion errors exceed 340 m, or the velocity insertion errors exceed 600 mm/s, the three stability indexes will not meet the requirement in Table 2. For the case of considering only tangential insertion errors, the permitted ranges of the position and velocity insertion errors are 40 km and 3 mm/s. Moreover, when considering only normal insertion errors, the permitted values of the position and velocity insertion errors are 140 km and 2.5 m/s, respectively. It was clearly found that the case of considering only normal insertion errors has the largest permitted ranges. As shown in Tables 7 and 8, this is due to the findings that neither the normal position insertion error nor the normal velocity insertion error impart a strong influence on the configuration stability.

Table 9. Permitted ranges of the stability domains.

Period	Case	Permitted Range	
		Position	Velocity
3 months	In all directions	340 m	3.4 mm/s
	Only radial direction	340 m	0.6 m/s
	Only tangential direction	40 km	3 mm/s
	Only normal direction	140 km	2.5 m/s
2 years	In all directions	21 m	0.4 mm/s
	Only radial direction	21 m	300 mm/s
	Only tangential direction	18 km	0.4 mm/s
	Only normal direction	45 km	900 mm/s

Furthermore, the maximal STDs of the arm length, the breathing angle and the relative velocity for a two-year mission lifetime under different insertion errors are also shown in Table 9. It can be seen that, compared with the three-month case, the maximal position insertion error decreases from 340 to 21 m, and the maximal velocity insertion error decreases from 3 mm/s to 0.4 mm/s. The stability domains of the two-year case considering only radial insertion errors, tangential insertion errors and normal insertion errors are illustrated in Table 9. For the two-year case considering only normal insertion errors, the position insertion errors should not exceed 45 km and the velocity insertion errors should not exceed 0.9 m/s.

The stability domains of different mission lifetimes are shown in Figure 15. It can be seen that the longer the mission lifetime, the smaller the stability domain. Considering the insertion errors under current techniques [12], the six-month mission is recommended.

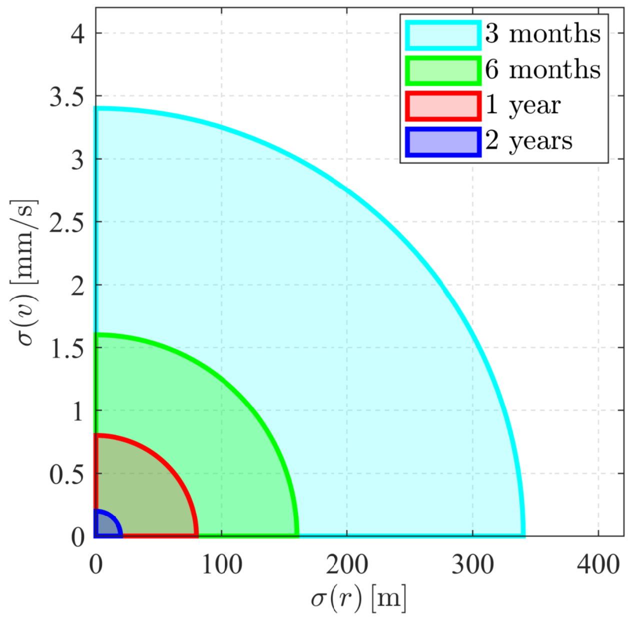

Figure 15. Stability domain of different mission life time.

5. Conclusions

This paper investigated the configuration uncertainty propagation problem of the geocentric gravitational-wave observatory using the unscented transformation (UT) method. It was found that the UT method with a UT tuning factor equal to −9 ($\kappa = 9$) has the best performance in predicting accuracy. Taking the Monte-Carlo simulation results as the standard, the UT method has relative errors of no larger than 2.7% with only 3.5697% of the computational consumption of the Monte Carlo method. Meanwhile, it was found that the radial position insertion errors and the tangential velocity insertion errors have the most significant effect on the configuration stability. The normal position and velocity insertion errors have the least effect on the stability. Furthermore, among the three stability indexes, the breathing angle is most likely to exceed the stability constraint. The stability domain of the geocentric gravitational-wave observatory is computed and analyzed. For a two-year mission lifetime, the configuration can remain stable if the standard deviation (STD) of the position insertion errors is no more than 21 m and the STD of the velocity insertion errors does not exceed 0.4 mm/s. The results in this paper can provide reference for the design of the navigation and control of the geocentric gravitational-wave observatory.

Author Contributions: Conceptualization, F.J. and X.L.; methodology and software, X.Z. All authors have read and agreed to the published version of the manuscript.

Funding: This work is sponsored by The National Key R&D Program of China (Grant No. 2020YFC2201200) and the Beijing Institute of Technology Research Fund Program for Young Scholars (Grant No. XSQD-202101012).

Data Availability Statement: Not applicable.

Acknowledgments: The authors thank Zhiyuan Cao for providing much-valued guidance.

Conflicts of Interest: The authors declare no conflict of interest.

References

1. Vatistas, G.H.; Lin, S.; Kwok, C.K. Reverse Flow Radius in Vortex Chambers. *AIAA J* **1986**, *24*, 1872–1873. [CrossRef]
2. Wu, W.; Tang, Y.; Zhang, L.; Qiao, D. Design of communication relay mission for supporting lunar-farside soft landing. *Sci. China Inf. Sci.* **2018**, *61*, 040305. [CrossRef]
3. Schaffer, S.; Chien, S.; Branch, A.; Hernandez, S. Automatic orbit selection for a radio interferometric spacecraft constellation. *J. Aerosp. Inf. Syst.* **2018**, *15*, 627–639. [CrossRef]

4. Martín, A.; Ibáñez, S.; Baixauli, C.; Blanc, S.; Belén Anquela, A. Multi-constellation GNSS interferometric reflectometry with mass-market sensors as a solution for soil moisture monitoring. *Hydrol. Earth Syst. Sci.* **2020**, *24*, 3573–3582. [CrossRef]
5. Cruz, R.J.; Thorpe, J.I.; Mueller, G. Laser interferometer space antenna simulator. *Laser Phys.* **2005**, *15*, 1056–1061.
6. Tang, Y.; Wu, W.; Qiao, D.; Li, X. Effect of orbital shadow at an Earth-Moon Lagrange point on relay communication mission. *Sci. China Inf. Sci.* **2017**, *60*, 112301. [CrossRef]
7. Ye, B.B.; Zhang, X.; Zhou, M.Y.; Wang, Y.; Yuan, H.M.; Gu, D.; Ding, Y.; Zhang, J.; Mei, J.; Luo, J. Optimizing orbits for TianQin. *Int. J. Mod. Phys. D* **2019**, *28*, 1950121. [CrossRef]
8. Shang, J.; Liu, J.; Poncos, V.; Geng, X.; Qian, B.; Chen, Q.; Dong, T.; Macdonald, D.; Martin, T.; Kovacs, J.; et al. Detection of crop seeding and harvest through analysis of time-series Sentinel-1 interferometric SAR data. *Remote Sens.* **2020**, *12*, 1551. [CrossRef]
9. Folkner, W.M.; Hechler, F.; Sweetser, T.H.; Vincent, M.A.; Bender, P.L. LISA orbit selection and stability. *Class. Quantum Gravity* **1997**, *14*, 1405. [CrossRef]
10. Wang, Y.; Zhang, Y.; Qiao, D.; Mao, Q.; Jiang, J. Transfer to near-Earth asteroids from a lunar orbit via Earth flyby and direct escaping trajectories. *Acta Astronaut.* **2017**, *133*, 177–184. [CrossRef]
11. Chen, Q.; Qiao, D.; Wen, C. Reachable domain of spacecraft after a gravity-assist flyby. *J. Guid. Control Dyn.* **2019**, *42*, 931–940. [CrossRef]
12. Luo, J.; Chen, L.S.; Duan, H.Z.; Gong, Y.G.; Hu, S.; Ji, J.; Liu, Q.; Mei, J.; Milyukov, V.; Sazhin, M.; et al. TianQin: A space-borne gravitational wave detector. *Class. Quantum Gravity* **2016**, *33*, 035010. [CrossRef]
13. Li, Z.; Zheng, J.; Li, M. Orbit insertion error analysis for a space-based gravitational wave observatory. *Adv. Space Res.* **2021**, *67*, 3744–3754. [CrossRef]
14. Hu, X.C.; Li, X.H.; Wang, Y.; Feng, W.F.; Zhou, M.Y.; Hu, Y.M.; Hu, S.C.; Mei, J.W.; Shao, C.G. Fundamentals of the orbit and response for TianQin. *Class. Quantum Gravity* **2018**, *35*, 095008. [CrossRef]
15. Li, X.; Qiao, D.; Li, P. Bounded trajectory design and self-adaptive maintenance control near non-synchronized binary systems comprised of small irregular bodies. *Acta Astronaut.* **2018**, *152*, 768–781. [CrossRef]
16. Zhou, X.; Cheng, Y.; Qiao, D.; Huo, Z. An adaptive surrogate model-based fast planning for swarm safe migration along halo orbit. *Acta Astronaut.* **2022**, *194*, 309–322. [CrossRef]
17. Cui, P.Y.; Qiao, D.; Cui, H.T.; Luan, E.J. Target selection and transfer trajectories design for exploring asteroid mission. *Sci. China Technol. Sci.* **2010**, *53*, 1150–1158. [CrossRef]
18. Han, H.; Qiao, D. Optimization for the aeroassisted orbital plane change with the synergetic maneuver using the hp-adaptive pseudospectral method. *J. Aerosp. Eng.* **2017**, *30*, 04017076. [CrossRef]
19. Yao, Q.; Han, H.; Qiao, D. Nonsingular Fixed-Time Tracking Guidance for Mars Aerocapture with Neural Compensation. *IEEE Trans. Aerosp. Electron. Syst.* **2022**, *58*, 3686–3696. [CrossRef]
20. Su, W.; Wang, Y.; Zhou, C.; Lu, L.; Zhou, Z.B.; Li, T.M.; Shi, T.; Hu, X.C.; Zhou, M.Y.; Wang, M.; et al. Analyses of Laser Propagation Noises for TianQin Gravitational Wave Observatory Based on the Global Magnetosphere MHD Simulations. *Astrophys. J.* **2021**, *914*, 139. [CrossRef]
21. Zhou, M.Y.; Hu, X.C.; Ye, B.; Hu, S.; Zhu, D.D.; Zhang, X.; Su, W.; Wang, Y. Orbital effects on time delay interferometry for TianQin. *Phys. Rev. D* **2021**, *103*, 103026. [CrossRef]
22. Han, H.; Qiao, D.; Chen, H.; Li, X. Rapid planning for aerocapture trajectory via convex optimization. *Aerosp. Sci. Technol.* **2019**, *84*, 763–775. [CrossRef]
23. Han, H.; Qiao, D.; Chen, H. Optimization of aeroassisted rendezvous and interception trajectories between non-coplanar elliptical orbits. *Acta Astronaut.* **2019**, *163*, 190–200. [CrossRef]
24. Yang, C.; Zhang, H. Formation flight design for a LISA-like gravitational wave observatory via Cascade optimization. *Astrodynamics* **2019**, *3*, 155–171. [CrossRef]
25. Chen, Q.; Qiao, D.; Wen, C. Orbital Element Reachable Set After Gravity Assists of Planets in Elliptical Orbits. *J. Guid. Control Dyn.* **2020**, *43*, 989–997. [CrossRef]
26. Luo, Y.Z.; Yang, Z. A review of uncertainty propagation in orbital mechanics. *Prog. Aerosp. Sci.* **2017**, *89*, 23–39. [CrossRef]
27. Qin, T.; Qiao, D.; Macdonald, M. Relative orbit determination using only intersatellite range measurements. *J. Guid. Control Dyn.* **2019**, *42*, 703–710. [CrossRef]
28. Qin, T.; Qiao, D.; Macdonald, M. Relative orbit determination for unconnected spacecraft within a constellation. *J. Guid. Control Dyn.* **2021**, *44*, 614–621. [CrossRef]
29. Qin, T.; Macdonald, M.; Qiao, D. Fully Decentralized Cooperative Navigation for Spacecraft Constellations. *IEEE Trans. Aerosp. Electron. Syst.* **2021**, *57*, 2383–2394. [CrossRef]
30. Zhou, X.; Wang, S.; Qin, T. Multi-Spacecraft Tracking and Data Association Based on Uncertainty Propagation. *Appl. Sci.* **2022**, *12*, 7660. [CrossRef]
31. Junkins, J.L.; Akella, M.R.; Alfriend, K.T. Non-Gaussian error propagation in orbital mechanics. *Adv. Astronaut. Sci.* **1996**, *92*, 283–298.
32. Vishwajeet, K.; Singla, P. Adaptive split/merge-based Gaussian mixture model approach for uncertainty propagation. *J. Guid. Control Dyn.* **2018**, *41*, 603–617. [CrossRef]
33. Geller, D.K. Linear covariance techniques for orbital rendezvous analysis and autonomous onboard mission planning. *J. Guid. Control Dyn.* **2006**, *29*, 1404–1414. [CrossRef]

34. Gelb, A.; Warren, R.S. Direct statistical analysis of nonlinear systems: CADET. *AIAA J* **1973**, *11*, 689–694. [CrossRef]
35. Julier, S.J.; Uhlmann, J.K. Unscented filtering and nonlinear estimation. *Proc. IEEE Inst. Electr. Electron. Eng.* **2004**, *92*, 401–422. [CrossRef]
36. Chang, L.; Hu, B.; Chang, G.; Li, A. Multiple outliers suppression derivative-free filter based on unscented transformation. *J. Guid. Control Dyn.* **2012**, *35*, 1902–1906. [CrossRef]
37. Adurthi, N.; Singla, P. Conjugate unscented transformation-based approach for accurate conjunction analysis. *J. Guid. Control Dyn.* **2015**, *38*, 1642–1658. [CrossRef]
38. Jones, B.A.; Doostan, A.; Born, G.H. Nonlinear Propagation of Orbit Uncertainty Using Non-Intrusive Polynomial Chaos. *J. Guid. Control Dyn.* **2013**, *36*, 430–444. [CrossRef]
39. Vishwajeet, K.; Singla, P.; Jah, M. Nonlinear Uncertainty Propagation for Perturbed Two-Body Orbits. *J. Guid. Control Dyn.* **2014**, *37*, 1415–1425. [CrossRef]
40. Jia, B.; Xin, M. Active Sampling Based Polynomial-Chaos–Kriging Model for Orbital Uncertainty Propagation. *J. Guid. Control Dyn.* **2021**, *44*, 905–922. [CrossRef]
41. Park, R.S.; Scheeres, D.J. Nonlinear semi-analytic methods for trajectory estimation. *J. Guid. Control Dyn.* **2007**, *30*, 1668–1676. [CrossRef]
42. Yang, Z.; Luo, Y.; Lappas, V.; Tsourdos, A. Nonlinear analytical uncertainty propagation for relative motion near J2-perturbed elliptic orbits. *J. Guid. Control Dyn.* **2018**, *41*, 888–903. [CrossRef]
43. Yang, Z.; Luo, Y.; Zhang, J. Nonlinear semi-analytical uncertainty propagation of trajectory under impulsive maneuvers. *Astrodynamics* **2019**, *3*, 61–77. [CrossRef]
44. Boone, S.; McMahon, J. Orbital guidance using higher-order state transition tensors. *J. Guid. Control Dyn.* **2021**, *44*, 493–504. [CrossRef]
45. Qiao, D.; Zhou, X.; Zhao, Z.; Qin, T. Asteroid Approaching Orbit Optimization Considering Optical Navigation Observability. *IEEE Trans. Aerosp. Electron. Syst.* **2022**. [CrossRef]
46. Zhou, X.; Qin, T.; Meng, L. Maneuvering Spacecraft Orbit Determination Using Polynomial Representation. *Aerospace* **2022**, *9*, 257. [CrossRef]
47. Tapley, B.D.; Watkins, M.M.; Ries, J.C.; Davis, G.W.; Eanes, R.J.; Poole, S.R.; Rim, H.J.; Schutz, B.E.; Shum, C.K.; Nerem, R.S.; et al. The joint gravity model 3. *J. Geophys. Res.* **1996**, *101*, 28029–28049. [CrossRef]